ACCSCIENCE PUBLISHING

International Journal of Bioprinting

RESEARCH ARTICLE

# 3D bioprinting of the glioblastoma microenvironment for preclinical assessment of CDK4/6 inhibition

**Philipp Kaps[1], Emily Zunke[1], Justus Ramtke[1], Christian Polley[2], Leonora Calopresti[2], Marcus Frank[3,4], Karoline Schulz[4], Piotr Grabarczyk[5], Sascha Troschke-Meurer[6], Charlotte Wagner[1], Annabell Wolff[1], Daniel Dubinski[7], Florian Gessler[7], Thomas M. Freiman[7], Christian Junghanss[1], Hermann Seitz[2,3], and Claudia Maletzki[1]***

[1]Department of Internal Medicine–Clinic and Polyclinic for Hematology, Hemostaseology, Oncology, Stem Cell Therapy and Palliative Medicine, Rostock University Medical Center, University of Rostock, Rostock, Germany

[2]Faculty of Mechanical Engineering and Marine Technology, University of Rostock, Rostock, Germany

[3]Department Life, Light & Matter, University of Rostock, Rostock, Germany

[4]Medical Biology and Electron Microscopy Centre, Rostock University Medical Center, University of Rostock, Rostock, Germany

[5]Department of Internal Medicine, Clinic III–Hematology, Oncology, University Medicine Greifswald, Greifswald, Germany

[6]Department of Pediatric Oncology and Hematology, University Medicine Greifswald, Greifswald, Germany

[7]Department of Neurosurgery, Rostock University Medical Center, University of Rostock, Rostock, Germany

***Corresponding author:**
Claudia Maletzki
(claudia.maletzki@med.uni-rostock.de)

**Citation:** Kaps P, Zunke E, Ramtke J, *et al.* 3D bioprinting of the glioblastoma microenvironment for preclinical assessment of CDK4/6 inhibition. *Int J Bioprint.* 2026:12(2):025520537. doi: 10.36922/IJB025520537

**Received:** November 27, 2025
**Revised:** December 28, 2025
**Accepted:** January 6, 2026
**Published online:** January 13, 2026



## Abstract

Glioblastoma (GBM) is an aggressive, World Health Organization grade 4 brain tumor with a poor prognosis, largely due to its complex, treatment-resistant microenvironment. To better model this environment for preclinical testing, we developed a three-dimensional (3D) biomimetic bioprinting platform using patient-derived GBM cells. Two hydrogels, alginate/gelatin (AlgGel; 1.5%/7.5%) and gelatin methacryloyl (10%), were evaluated for biocompatibility. GBM cells (GBM06, GBM14, and GBM15), transduced with iRFP-680 for viability tracking, were embedded in the hydrogels and printed. Tumor growth and viability were monitored for 28 days using fluorescence microscopy, complemented by electron microscopy (EM) for structural analysis. Drug response testing included temozolomide (TMZ; 10 μM) and the cyclin-dependent kinases 4/6 inhibitor abemaciclib (1 μM). Cell viability and extracellular vesicle (EV) release were quantified. Efficacy was further assessed in a co-culture with astrocytes. The AlgGel hydrogel supported superior long-term viability and growth. EM analysis of AlgGel scaffolds revealed preserved cellular architecture and adherence to the bioprinted extracellular matrix. Drug response assays confirmed findings previously observed in 2D and 3D cultures. Two cycles of abemaciclib reduced GBM cell viability in AlgGel scaffolds, accompanied by a significant decrease in EV secretion. TMZ, in contrast, did not significantly affect cell viability. The reduction in viability remained pronounced in co-culture with astrocytes, without compromising astrocyte viability. In this study, we present a

3D biomimetic bioprinting model that successfully mimics key aspects of the GBM microenvironment. This model demonstrates strong potential as a preclinical drug screening tool, enabling improved mechanistic insight into cell–matrix interactions that govern nutrient/metabolite diffusion and therapeutic responses.

***Keywords:*** Abemaciclib; Alginate–gelatin hydrogel; CDK4/6 inhibition; Cell–matrix interaction; Glioblastoma; Patient-derived tumor cells; Three-dimensional culture; Tumor microenvironment

## 1. Introduction

As the most prevalent malignant brain tumor, glioblastoma (GBM) accounts for the majority of primary brain tumor-related mortality.[1,2] This high mortality rate is partly due to the lack of effective treatment regimens capable of achieving complete tumor remission. Therefore, the development of novel therapeutic strategies is essential to improve the poor prognosis of patients with GBM.

The development and application of new drugs typically follow an extensive, multifaceted pipeline, beginning with the identification of promising compounds, progressing through rigorous preclinical testing, and ultimately culminating in clinical trials.[3] The transition from preclinical to clinical testing often fails, in part due to the inability of preclinical models to adequately recapitulate the complex conditions observed in patients. Consequently, current GBM models frequently fail to predict drug efficacy and patient-specific responses. Three-dimensional (3D) models can address this challenge by better simulating *in vivo* conditions, preserving cell morphology, supporting cell–cell interactions,[4] reflecting key factors like diffusion-limited nutrient and oxygen transport,[5] and exhibiting increased drug resistance compared to two-dimensional (2D) models.[6,7]

One of the most versatile and promising 3D modeling techniques is 3D bioprinting, which allows for precise spatial placement of cells within biomaterials that mimic the natural extracellular matrix (ECM), facilitating crucial cellular interactions.[8] A variety of biomaterials, such as alginate, gelatin, and modifications of these biomaterials like gelatin methacryloyl (GelMa), have been successfully used to create bioinks that generate structurally stable scaffolds, allowing tumor cells to attach, proliferate, and form complex structures.[9–11] These biomimetic models offer a more physiologically relevant platform compared to conventional 2D models for studying GBM pathobiology in a clinically relevant context.

In this study, we present a straightforward 3D bioprinting model for GBM using two hydrogels—alginate/gelatin (AlgGel) and GelMa hydrogels. AlgGel demonstrated favorable biocompatibility and facilitated the formation of a supportive matrix that closely resembles the natural tumor microenvironment (TME). In a preclinical pilot study, 3D-bioprinted GBM cells exhibited intrinsic resistance to the standard-of-care drug temozolomide (TMZ), but responded well to abemaciclib, a cyclin-dependent kinase (CDK) 4/6 inhibitor currently undergoing Phase 2 and Phase 3 trials for both primary and recurrent GBM (clinicaltrials.gov IDs: NCT02981940, NCT06413706, and NCT02977780).

With this approach, we aim to bridge the gap in preclinical testing by providing a more accurate and clinically relevant model, which could significantly contribute to the development of novel and more effective GBM therapies.

## 2. Methods

### 2.1. Bioink preparation

The bioink was prepared by dissolving 3% (w/v) alginate (Carl Roth, Germany) or 15% (w/v) gelatin (Sigma-Aldrich, USA) in phosphate-buffered saline (PBS; PAN-Biotech, Germany) while stirring at 250 rpm and 37°C overnight. Alginate and gelatin solutions were then mixed at a 1:1 ratio by stirring at 250 rpm for 1 h.

For the GelMa hydrogel, 0.5% (w/v) lithium phenyl-2,4,6-trimethylbenzoylphosphinate was dissolved in PBS (pH = 7.4) at 37°C by stirring at 250 rpm for 30 min while protected from light. Next, 10% (w/v) lyophilized GelMa was added and stirred for 60 min until a homogeneous solution was obtained.

### 2.2. Rheological characterization

The rheological properties of AlgGel and GelMa hydrogels were assessed using an Anton Paar MCR 302 rheometer (Anton Paar Germany GmbH, Germany) equipped with a 25 mm cone-plate setup and a gap of 0.05 mm. Rotational rheometry was performed with an increasing shear rate from 0.01–1000 $s^{-1}$ at 22°C. Oscillating amplitude sweeps were performed to determine the yield stress required to

initiate flow during 3D printing. Sweeps were conducted at a frequency of 10 rad/s with a logarithmic increase of shear deformation from 1% to 1000%. Data were collected at 10 points per decade. The crossover point between the storage modulus G' and the loss modulus G" (loss factor tan $\delta$ = G"/ G' = 1) was used to define the yield point. All measurements were performed in triplicate ($n$ = 3). Data were plotted and analyzed using Origin 2024 software (OriginLab Corp., USA).

### 2.3. Cell culture

Patient-derived GBM cell lines (GBM06, GBM14, and GBM15) were established from tumor specimens of World Health Organization grade 4 GBM patients (Table 1). These samples were obtained from the Department of Neurosurgery at the University Medical Center Rostock, Germany, with informed consent obtained from all patients. All procedures were approved by the local Ethics Committee (Rostock University Medical Center, Ethics Registration ID: A2018-0167) and conducted in accordance with widely accepted guidelines for the use of human materials.

Cell lines were cultured in Dulbecco's Modified Eagle Medium/Nutrient Mixture F-12 (DMEM/F12) supplemented with 10% fetal calf serum, 6 mmol/L L-glutamine, and 1% penicillin/streptomycin (all from PAN-Biotech, Germany). Human astrocytes (hAstro) were purchased from ScienCell (USA) and cultured in astrocyte medium supplemented with 5% fetal calf serum, 1% penicillin/streptomycin, and 1× astrocyte growth supplement (all from ScienCell, USA) on poly-L-lysine-coated vessels. Cells were incubated at 37°C in a humidified atmosphere containing 5% $CO_2$. In some experiments, tumor cells were transduced with a lentiviral vector to stably express a near-infrared fluorescent protein (iRFP680).[12,13]

### 2.4. Three-dimensional bioprinting

The prepared hydrogels were pre-warmed in a water bath at 37°C, and tumor cells were suspended in the warmed hydrogels at a concentration of $1 \times 10^6$ cells/mL. The final bioinks were transferred into a cartridge and placed in the cartridge holder. Scaffolds were printed into 12-well plates as grids consisting of three layers, each with a layer height of 0.25 mm.

For AlgGel scaffolds, the plates were coated with poly-D-lysine (Sigma-Aldrich, USA). The AlgGel bioink was printed using the Allevi 1 Bioprinter (Allevi, USA). The cartridge was tempered to 26°C before printing. The bioink was extruded through a 250 µm nozzle at a speed of 8 mm/s to print grid-like scaffolds. Extrusion pressure was adjusted between 70–110 kPa based on filament formation. Scaffolds were crosslinked by incubation in 0.1 M calcium chloride ($CaCl_2$) for 10 min at room temperature, after which the supernatant was replaced with cell culture medium.

The GelMa scaffolds were printed using the GeSiM Bioscaffolder 3.3 (GeSiM, Germany). The bioink was tempered to 22°C prior to printing. Printing was performed using a 250 µm nozzle at a speed of 1.8 mm/s, and an extrusion pressure of 80–100 Pa. GelMa scaffolds were crosslinked by ultraviolet (UV) irradiation for 3 s. After printing, cell culture medium was added, and the cell-laden scaffolds were incubated at 37°C in a humidified 5% $CO_2$ atmosphere.

### 2.5. Electron microscopy

After 10 days of incubation, cell-laden scaffolds containing GBM14 were washed with 0.1 M 4-(2-hydroxyethyl)-1-piperazineethanesulfonic acid (HEPES) buffer (pH 7.4), fixed with 2.5% glutaraldehyde in 0.1 M HEPES buffer for 2 h, and stored at 4°C. Following fixation, scaffolds were

**Table 1. Clinical characteristics of patient-derived glioblastoma cell lines**

| Patient ID | Gender, age (years) | Location | *MGMT* gene status | Therapy/outcome | Mutations |
|---|---|---|---|---|---|
| GBM06 | Male, 71 | Temporal lobe | Methylated | Radiotherapy/3.6 months[a] | *TP53* G244A (VAF: 99.0%); P72R (VAF: 100.0%); *PIK3CA* I391M (VAF: 30.0%) |
| GBM14 | Male, 63 | Left temporal lobe | Unmethylated | Radio-chemotherapy/27.4 months[a] | *TP53* V173L (VAF: 58.6%); P72R (VAF: 58.3%); *KDR* Q472H (VAF: 54.0%); *PTEN* D252Y (VAF: 100.0%) |
| GBM15 | Male, 40 | Left parietal lobe | Unmethylated | Radio-chemotherapy/2.5 months[a] | *TP53* P72R (VAF: 99.0%) |

Note: All specimens were diagnosed as World Health Organization grade 4 glioblastoma with a wild-type isocitrate dehydrogenase status.

[a]Time of survival after initial diagnosis.

washed with 0.1 M HEPES buffer and postfixed in 1% osmium tetroxide in 0.05 M HEPES buffer. After rinsing with 0.1 M HEPES buffer, scaffolds were dehydrated using a graded acetone series, starting with 50% acetone in 0.05 M HEPES buffer for 5 min, followed by 70%, 90%, and 100% acetone for 30 min each. After an additional acetone exchange, samples were either processed for resin embedding for transmission electron microscopy (TEM) inspection or kept in 100% acetone for air-drying with desiccation for scanning electron microscopy (SEM) analysis, respectively.

Resin infiltration began with a 1:1 mixture of Epon resin (Serva, Germany) and acetone overnight in a fume hood, and was completed with pure resin the following day. Specimens were transferred to rubber molds containing a layer of pre-cured Epon resin as a spacer and cured in an oven for at least 48 h prior to trimming and sectioning with an ultramicrotome using a diamond knife, as described in previous research.[14] Thin sections (approximately 70 nm) were contrasted with lead citrate and uranyl acetate for ultrastructural inspection using a Zeiss EM 902 electron microscope operated at 80 kV (Zeiss, Germany). Semi-thin sections (0.5–1 μm) were stained with toluidine blue for light microscopy to visualize cells and the sample matrix, using a Zeiss Axioscope 40 equipped with an ERc 5s digital camera (Zeiss, Germany) and Zeiss ZEN Blue software (version 2.0, Zeiss, Germany) for acquisition.

For SEM analysis, dried samples were mounted on standard aluminum SEM holders using conductive carbon pads (Plano GmbH, Germany) and coated with a 6-nm carbon layer to ensure surface conductivity (coating unit CCU-010, Safematic, Switzerland). Imaging was performed using a field emission SEM (Zeiss Merlin VP compact, Zeiss, Germany) at an accelerating voltage of 5 kV, employing secondary electron and in-lens detection modes.

### 2.6. *In vitro* dose–response study

To test the sensitivity of GBM cells to abemaciclib, cells were seeded at a density of 5000 cells/well in 96-well plates (Greiner Bio-One, Austria) under 2D culture conditions and incubated at 37°C in a humidified 5% $CO_2$ atmosphere. After 24 h, cells were treated with escalating doses of abemaciclib for two cycles of 72 h. After a total of 144 h, cell viability was evaluated using the crystal violet assay. Briefly, cells were washed with PBS and stained with 0.2% crystal violet solution for 10 min. Wells were then washed twice with PBS, and crystal violet was dissolved by adding 1% sodium dodecyl sulfate for 10 min to quantify biomass. Absorbance was measured using a Tecan Infinite 200 Pro M Plex (Tecan Group AG, Switzerland) at 570 nm, with 620 nm as the reference wavelength.

### 2.7. Compound treatment

Scaffolds were treated 7 days after printing. Cell culture medium was replaced with medium containing either abemaciclib (1 μM), TMZ (10 μM), or dimethyl sulfoxide as a control. This procedure was repeated after 72 h. Cell viability was analyzed microscopically using a Zeiss Axio Vert.A1 fluorescence microscope equipped with a Colibri 5 LED (Zeiss, Germany). Fluorescence intensity of iRFP680-transduced cells was used as a viability marker and quantified using ImageJ software (v1.54p, National Institutes of Health, USA).

### 2.8. Isolation and analysis of extracellular vesicles

Extracellular vesicles (EVs) were isolated from the supernatant of scaffolds on days 3 and 6 of treatment. The supernatant was diluted to 1 mL and centrifuged at 400 × g for 10 min. After centrifugation, 900 μL of the supernatant was transferred to new 1.5 mL tubes and centrifuged at 14,000 × g for 30 min. Subsequently, 800 μL of supernatant was removed. The remaining liquid was diluted to 1 mL and centrifuged again at 14,000 × g for 30 min. This step was repeated once more, after which 900 μL of supernatant was removed. Finally, EVs were resuspended in the remaining 100 μL and stored at −80°C until analysis.

For the quantification, EVs were diluted 1:10 in PBS and were analyzed for particle concentration and size using nanoparticle tracking analysis with the NanoSight® LM10 instrument (Malvern Instruments Ltd., United Kingdom). Particle concentration from a PBS blank was subtracted from the sample concentration to account for background particles in the PBS.[15]

### 2.9. Spectral flow cytometry of extracellular vesicles

For flow cytometric analysis, EV suspensions were adjusted to concentrations between $3 \times 10^7$ and $5 \times 10^9$ particles. To identify membrane-enclosed EVs, samples were stained with the Pacific Blue ExoBrite™ True EV Membrane Stain (1:500; catalog no. 30136-T, Biotium, USA) in combination with 1:500 phycoerythrin-cyanine 7–conjugated anti-human CD9 (clone HI9a; stock 50 μg/mL; catalog no. 312116), CD63 (clone H5C6; stock 200 μg/mL; catalog no. 353010), and CD81 (clone 5A6; stock 200 μg/mL; catalog no. 349512) (BioLegend, USA).

For further surface phenotyping, the following antibodies were included: Brilliant ultra violet (BUV)496-conjugated antihuman Cluster of differentiation 109 (CD109) (Transforming growth factor β (TGF-β), clone (TEA2)/16, stock 0.2 mg/ mL, Becton Dickinson (BD), 1:500), BUV615-conjugated anti-human, Epidermal growth factor receptor (EGFR) (clone Cetuximab297. rMAb, stock 0.2 mg/mL, BD, 1:500), RY610-conjugated anti-human CD95 (Fas, clone DX2, stock 100 μg/mL, BD,

1:250), Alexa Fluor® 647-conjugated anti-human THSB-1 (clone C-8, stock 200 µg/mL, Santa Cruz, 1:250), and BUV737-conjugated anti-human CD261 (tumor necrosis factor-related apoptosis-inducing ligand [TRAIL]-R1, clone S35-934, stock 0.2 mg/mL, BD, 1:160).

For staining, ExoBrite and all antibodies were premixed and centrifuged at 10,000 × g for 10 min to remove fluorochrome or antibody aggregates. A total volume of 250 µL staining solution was added to each EV preparation and incubated for 30 min at room temperature. Measurements were performed using a Sony ID7000 flow cytometer. EVs were defined as ExoBrite$^+$/tetraspanin$^+$ events, and marker expression was analyzed within this population.

To ensure the specificity and reliability of EV detection, multiple controls were included: PBS controls with and without dyes or antibodies, unstained EVs, antibody titration controls, and serial dilutions to exclude swarm effects. Tumor cell and PBMC (Peripheral blood mononuclear cells) samples were used to verify marker localization. A detergent control was performed to confirm that the detected signals originated from membrane-bound structures.

### 2.10. Co-culture of patient-derived glioblastoma cells with human astrocytes

hAstro were labeled with CellTrace Violet (Thermo Fisher Scientific, USA) prior to printing. For staining, $1 \times 10^6$ cells were harvested and centrifuged at 300 × g for 5 min. The pellet was resuspended in pre-warmed PBS containing 5 µM CellTrace Violet and incubated for 20 min at 37°C, protected from light. Subsequently, cells were diluted with five times the original staining solution volume of complete astrocyte medium and incubated for an additional 5 min. After centrifugation at 300 × g for 5 min, the stained hAstro were mixed at a ratio of 1:1 with GBM cells in the AlgGel hydrogel, resulting in a final concentration of $2 \times 10^6$ cells/mL.

The bioink preparation and printing procedure followed the conditions described above. Printed scaffolds were cultured in a 1:1 mixture of DMEM/F12 complete medium and Astrocyte complete medium. Viability of untreated and treated co-cultures was monitored by fluorescence microscopy for up to 28 days.

### 2.11. Immunofluorescence

Immunofluorescence of the co-culture was performed using two approaches.

(a) Cryosection-based staining

Scaffolds containing unlabeled cells were washed twice with 25 mM HEPES (4-(2-hydroxyethyl)-1-piperazineethanesulfonic acid) containing 10 mM $CaCl_2$, followed by fixation in 4% paraformaldehyde prepared in 25 mM HEPES, 10 mM $CaCl_2$, and 150 mM sodium chloride for 30 min. After fixation, scaffolds were washed twice with the same buffer and incubated in 10% sucrose prepared in this buffer for 2 h, followed by overnight cryoprotection in 30% sucrose.

The next day, scaffolds were embedded in TissueTek, snap-frozen in liquid nitrogen, and sectioned at 6 µm thickness. Sections were fixed with ice-cold methanol, washed three times with PBS, and blocked with 2% bovine serum albumin (BSA) for 1 h at room temperature.

Primary antibody incubation was performed overnight at 4°C in 2% BSA/PBS using the following antibodies: Alexa Fluor® 488 anti-nestin (RRID:AB_2723399, catalog no. MA1-110-A488, Thermo Fisher Scientific, USA), Alexa Fluor® 594 anti-vimentin (1:200, RRID:AB_2566179; catalog no. 677804, BioLegend, USA), DyLight 550 anti-S100B (RRID:AB_3284201; catalog no. 18794752, Novus Biologicals, USA), and FL650 anti-ALDH1L1 (RRID:AB_2939519; catalog no. 75-140-FL650, Antibodies Incorporated, USA).

Nuclear counterstaining was carried out using 4',6-diamidino-2-phenylindole–containing mounting medium (Carl Roth, Germany). Fluorescence images were acquired using a Zeiss AX10 (Vert.A1) fluorescence microscope.

(b) Whole-mount scaffold staining

Intact scaffolds containing labeled cells were fixed with 4% paraformaldehyde prepared in 25 mM HEPES, 10 mM $CaCl_2$, and 150 mM sodium chloride for 30 min and washed three times with 25 mM HEPES and 10 mM $CaCl_2$. Scaffolds were permeabilized and blocked for 1 h in 0.5% Triton X-100 (Sigma-Aldrich, USA) and 1% BSA prepared in 25 mM HEPES and 10 mM $CaCl_2$. Primary staining was performed overnight at 4°C using Alexa Fluor® 594 anti-vimentin (1:200) diluted in 1% BSA, 25 mM HEPES, and 10 mM $CaCl_2$. After washing, scaffolds were microscopically examined using a Zeiss LSM 910 confocal laser-scanning microscope (Zeiss, Germany).

### 2.12. Statistical analysis

Quantified data are presented as mean ± standard deviation. Statistical analyses were conducted using GraphPad Prism software (version 8.0.2, GraphPad Software, USA; RRID:SCR_002798). Data were tested for normality using the Shapiro–Wilk test. As all datasets followed a normal distribution, parametric statistical analyses were performed using appropriate tests, such as unpaired *t*-test, one-way ANOVA, two-way ANOVA, Tukey multiple comparisions test and Dunnett's multiple

comparisions test (for post-hoc analysis). A $p$-value of <0.05 was considered statistically significant.

## 3. Results

### 3.1. Bioinks exhibit rheological properties suitable for bioprinting

Bioinks for extrusion-based bioprinting must meet key criteria, including cytocompatibility, shape fidelity, and printability.[16,17] Their rheological properties must ensure extrudability while balancing viscosity, required extrusion pressure, and rapid recovery of structural integrity after extrusion to enable a layer-by-layer process.[18,19]

To fabricate the GBM models, we investigated the rheological properties of AlgGel and GelMa bioinks (Figures S1 and S4A). Both hydrogels exhibited comparable rheological behavior, showing a linear decrease in viscosity with increasing shear rate. This shear-thinning behavior is essential for extrusion through the printer nozzle (Figure 1A).[19] AlgGel exhibited a significantly higher viscosity than GelMa across all applied shear rates. This difference was also reflected in the oscillatory measurements, where both the G' and G" moduli of AlgGel exceeded those of GelMa.

Both materials exhibited solid-like behavior at low shear stress, although viscous (liquid-like) components were more pronounced in AlgGel. In contrast, GelMa exhibited the typical behavior of gelatin, with a dominant G', indicating a predominance of solid-like properties (Figure 1B). The ability of gelatin to behave as an elastic solid at room temperature and its high thermo-responsiveness allow precise tuning of bioink properties, enabling a balance between extrudability and stackability.[20]

However, both inks begin to flow under shear stress, indicating structural breakdown at the yield point. The yield point is reached much earlier with GelMa than with the higher-viscosity AlgGel (Figure 1C). GelMa, at the concentration used, begins to flow earlier than the AlgGel ink, which indicates better printability and potentially lower shear stress on cells during extrusion, as the shear stresses developing on the nozzle walls are lower. However, no significant differences in shape fidelity or immediate post-printing cell viability were observed for either material. Crosslinking was necessary in both cases to establish the integrity of the printed gels, with AlgGel crosslinked by $Ca^{2+}$ ions and GelMa by UV illumination.

### 3.2. Patient-derived GBM cells proliferate in bioprinted AlgGel, but not in GelMa scaffolds

To examine the printability and viability of patient-derived GBM cells, three GBM cell lines with distinct molecular profiles were used: GBM06$^{MGMT\text{meth}}$, GBM14$^{MGMT\text{unmeth}}$, and GBM15$^{MGMT\text{unmeth}}$. iRFP680-transduced cells were mixed with AlgGel or GelMa hydrogels and printed as mesh-like scaffolds in 12-well plates (Figure 2A). The mesh design facilitated nutrient diffusion within the scaffold.

Cell viability was analyzed by fluorescence microscopy, as only viable cells express the fluorescent iRFP680 protein (Figures 2C and S2). Microscopic imaging revealed a uniform cell distribution within both hydrogels, with most cells remaining viable immediately after printing, as evidenced by strong fluorescence signals. No significant scaffold degradation or structural changes were observed

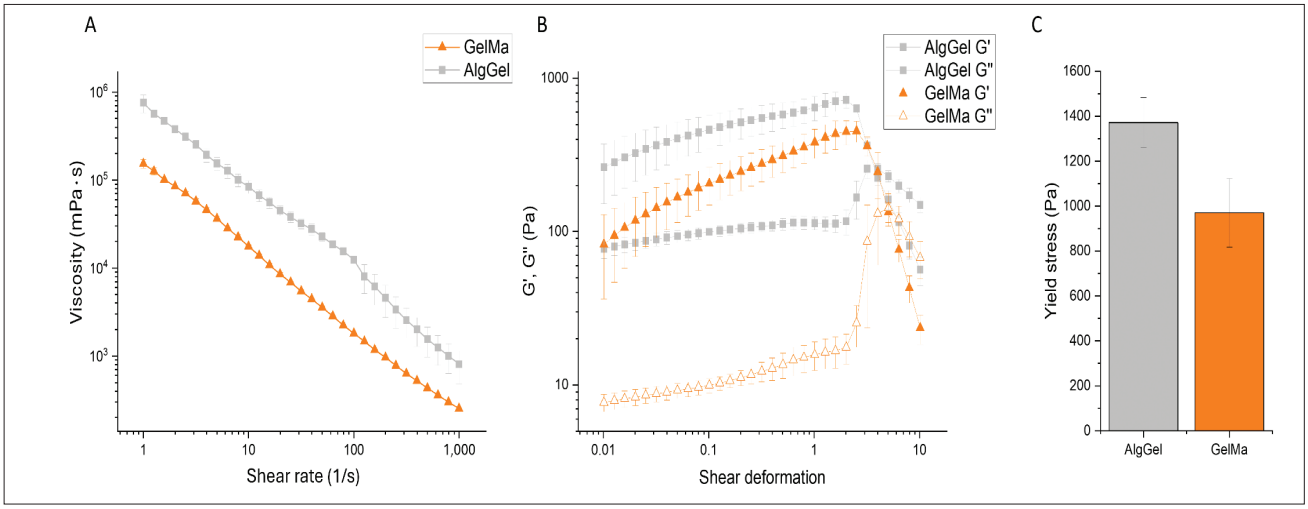


**Figure 1.** Characterization of rheological properties of AlgGel and GelMa inks used for glioblastoma model fabrication. (A) Dynamic viscosity vs. shear rate from rotational measurements ($n$ = 3 per material, mean ± standard deviation). (B) Oscillatory amplitude sweeps showing storage and loss moduli versus shear deformation ($n$ = 3 per material, mean ± standard deviation). (C) Yield stress determined from the oscillatory measurements (G' = G"). All measurements were conducted at 22°C. Abbreviations: G', storage modulus; G", loss modulus; AlgGel, alginate–gelatin; GelMa, gelatin methacryloyl.

over time in either AlgGel or GelMa, indicating a stable microenvironment.

Long-term cell viability was monitored over a period of 28 days and quantified based on fluorescence intensity measurements (Figure 2D). GBM06 and GBM14 showed increasing fluorescence signals in AlgGel scaffolds, indicating active cell proliferation. GBM15 showed no increase in fluorescence, leading to the termination of observation after 14 days and, consequently, the exclusion of this cell line from further experiments. iRFP680-fluorescent GBM06 cells printed in GelMa (Figure 2B) showed no increase in fluorescence, with the signal plateauing and subsequently declining by day 28 (Figure 2E and F). Additionally, GelMa hydrogels exhibited a high background fluorescence signal, complicating the detection of cell-derived signals; therefore, no further experiments were conducted using the GelMa composition.

Overall, these findings indicate that the bioprinted GBM cells not only survive the printing process but also remain viable and, in most cases, proliferate within the 3D-printed

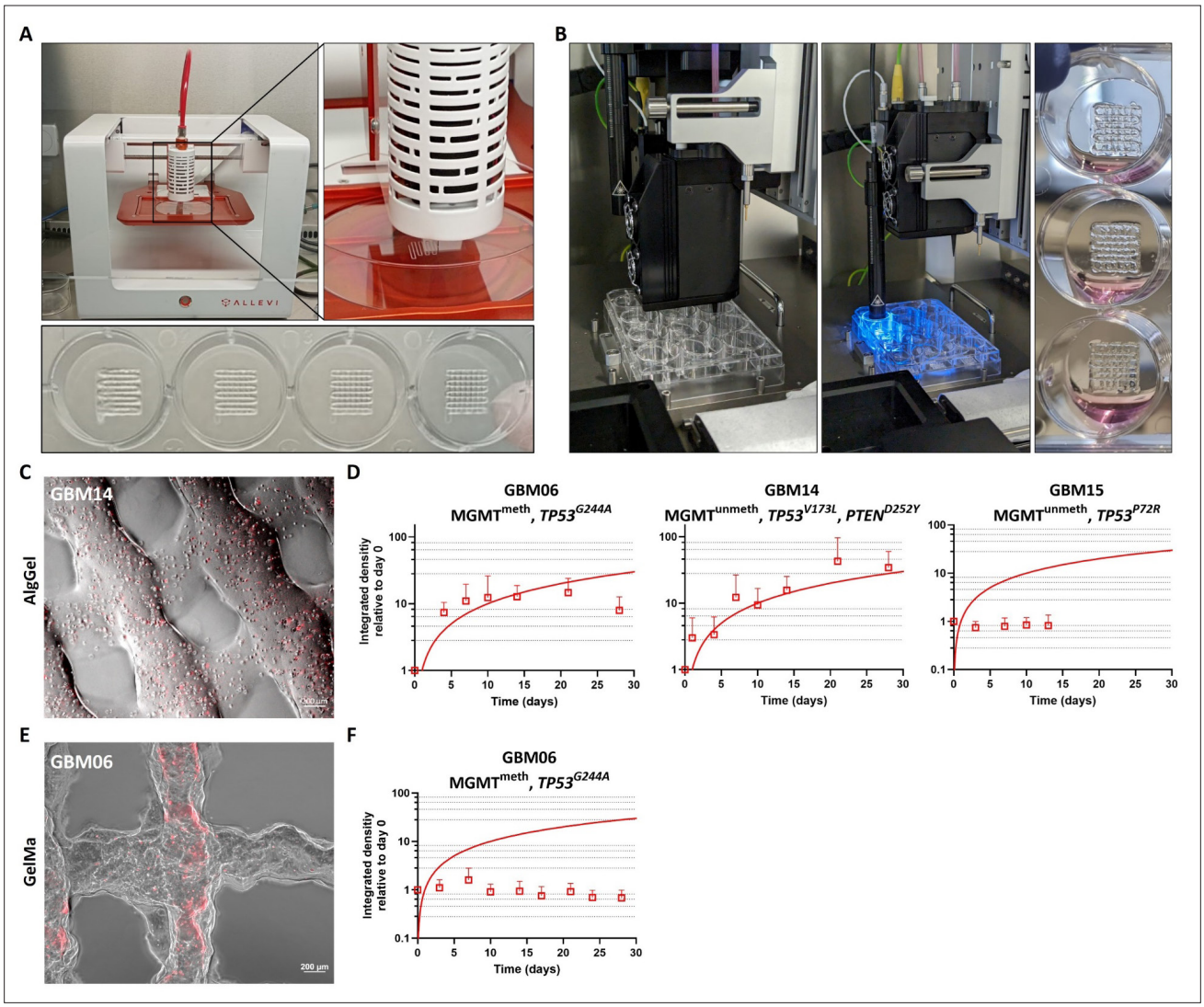


**Figure 2.** Bioprinting of AlgGel and GelMa hydrogels with GBM cells. (A, B) Overview of the bioprinting process using the (A) Allevi 1 bioprinter for the 1.5% alginate/7.5% gelatin (w/v) scaffolds and (B) GeSim Bioscaffolder 3.3 for 10% GelMa (w/v) scaffolds. Bioinks were printed as mesh-like scaffolds consisting of three layers, each with a height of 0.25 mm, and crosslinked with (A) 0.1 M calcium chloride solution or (B) ultraviolet light irradiation for 3 s. (C–F) Viability of printed GBM cells was assessed at different time points after printing. Tumor cells were transduced with a lentiviral vector to express the fluorescent iRFP680 protein prior to printing. (C, E) Fluorescence of living cells was captured using a fluorescence microscope (scale bar = 200 µm; magnification: 3.15×). (D, F) Viability of different patient-derived GBM cell lines was monitored for up to 28 days in either (D) AlgGel or (F) GelMa. Due to high background signal in GelMa scaffolds, which impaired quantification, only GBM06 cells were printed with the GelMa bioink ($n$ = 7, mean ± standard deviation). Abbreviations: AlgGel, alginate–gelatin; GBM, glioblastoma; GelMa, gelatin methacryloyl.

scaffolds over a period of 28 days. However, the choice of the hydrogel is crucial for GBM growth; in this case, the AlgGel composition outperformed GelMa. Accordingly, subsequent functional analyses were performed using AlgGel bioprints.

### 3.3. Cellular integrity is maintained after the printing process

We conducted SEM and TEM analyses to investigate how the bioprinting process affects GBM cell integrity and cell–scaffold interactions within the 3D AlgGel scaffold (Figure 3). Toluidine blue-stained semi-thin sections from embedded specimens (Figure 3A–C) exhibited a uniform distribution of GBM14 cells throughout the scaffold, with cells appearing fully encapsulated by the hydrogel. Although minor artifacts, such as differential shrinkage between cells and the matrix, were observed due to the dehydration and resin infiltration processes (Figure 3B), the overall morphology indicated that cellular integrity was preserved post-printing. SEM imaging provided detailed views of both the surface and internal regions of the bioprinted scaffolds while maintaining structural relationships (Figure 3D–F).

Analysis of the scaffold (Figure 3D) revealed numerous embedded tumor cells not only at the surface but also deep within the core of the sectioned scaffold, confirming successful cell incorporation and homogeneous distribution throughout the construct. Higher-magnification images (Figure 3E and F) showed individual embedded cells with intact membrane surfaces, further suggesting that the bioprinting process did not compromise cellular viability and largely maintained structural integrity. TEM analysis offered additional ultrastructural insights (Figure 3G–I). Thin sections revealed cells residing within hydrogel cavities, displaying multiple preserved organelles, vesicles, and short microvilli-like processes emerging from intact cell membranes (Figure 3G and H).

Notably, the presence of a cilium (Figure 3I) indicates cellular viability and suggests the maintenance of specific cellular structures post-printing. Some intracellular damage observed was attributed to the disproportionately large shrinkage of the AlgGel matrix during dehydration and resin embedding. However, the porous architecture and crosslinked network of the AlgGel matrix, which are essential for cell anchorage and nutrient diffusion, were evident in both SEM and TEM images (Figure S3).

Together, these findings indicate that the 3D bioprinting process does not negatively affect tumor cell integrity and that the AlgGel scaffold supports uniform cellular distribution and structural preservation post-printing.

### 3.4. The CDK4/6 inhibitor abemaciclib sustainably reduces the viability of 3D-bioprinted GBM cells

Our 3D bioprinting model was then used for preclinical drug testing with TMZ and abemaciclib (Figure 4). Abemaciclib has been employed in prior research and is currently under clinical investigation in Phase 2 and Phase 3 studies for primary and recurrent GBM.[14,21,22]

To confirm the efficacy of abemaciclib against iRFP680-transduced GBM cells, we performed a dose–response study on 2D cultures. Cells exposed to increasing doses of abemaciclib for two cycles of 72 h (Figure 4A) exhibited ≥20% growth reduction at all doses ($IC_{20}$). Additionally, mitochondrial DNA content, a marker for cell viability, was quantified (Figure 4A). In both cell lines, the mitochondrial DNA content was observed to be significantly lower compared to the controls.

For the 3D-bioprinted model, cells printed in AlgGel scaffolds were treated with TMZ (10 µM) and abemaciclib (1 µM) for two cycles of 72 h (Figure 4B and C). Microscopic examination revealed reduced fluorescence intensity after abemaciclib treatment, indicating decreased cell viability (Figure 4B). Quantification of fluorescence intensity (Figure 4C) further supported these findings, showing significantly reduced cell viability over time in both GBM06 and GBM14 cell lines (day 3: $p < 0.05$ vs. control). Viability reduction in GBM14 cells was even more pronounced in the 3D model than in the 2D cultures, suggesting increased sensitivity in the 3D bioprinting model.

Both cell lines were unable to recover from abemaciclib-induced cellular stress, and viability remained below control levels over the 23-day follow-up period. In contrast, TMZ had a negligible impact on cellular viability, slightly reducing viability in GBM14 only after the first treatment cycle. During the post-treatment follow-up period, TMZ showed no lasting effect, with fluorescence intensity ultimately returning to levels comparable to control cells. These results confirm that abemaciclib retains therapeutic efficacy in the 3D-bioprinted GBM model. Notably, therapeutic effects were detectable even in the GelMa hydrogel, despite impaired growth in the control scaffolds (see Figure S4A).

As an additional biomarker of response, EV secretion into the supernatant of GBM14 scaffolds was analyzed (Figure 4D). Supernatants were collected at days 3 and 6 post-treatment to examine the potential effects of TMZ and abemaciclib on EV release and characteristics (Figure 4E). After the first cycle of abemaciclib, EV particle concentration was significantly reduced by more than

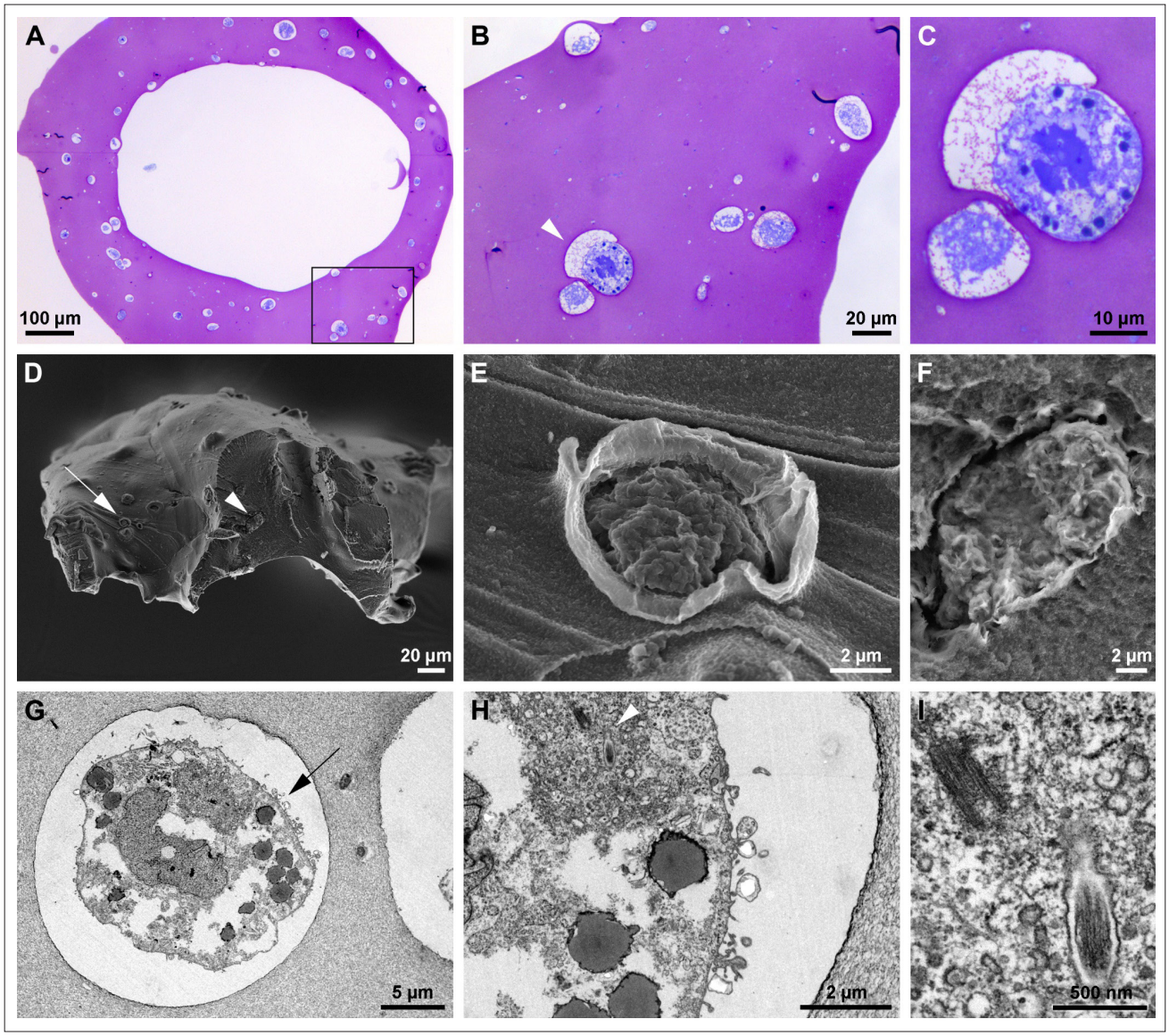


**Figure 3.** Microscopic examination of printed scaffolds with glioblastoma cells. After 10 days, scaffolds were analyzed microscopically. (A–C) Semi-thin sections (approximately 1 µm) of the printed scaffolds were stained with toluidine blue to differentiate the matrix from cells and to visualize embedded cells (arrowheads) prior to transmission electron microscopy (TEM) analysis. Images are shown at increasing magnifications: (A) scale bar = 100 µm; magnification: 100×, (B) scale bar = 20 µm; magnification: 400×, and (C) scale bar = 10 µm; magnification:1000×. (D–F) Representative scanning electron microscopy images of scaffold surface (arrow) and fractured scaffold revealing the core (arrowhead; D), enabling direct visualization of individual cells (E, F). Images are shown at the following scale bars and magnifications: (D) scale bar = 20 µm; magnification: 350× and (E) scale bar = 2 µm, magnification: 8000×, (F) scale bar = 2 µm, magnification: 4000×. (G–I) TEM analysis of cellular ultrastructure. A representative single cell (G) displays an intact membrane and microvilli-like processes (arrow). Intracellular organelles, including lysosomes, multivesicular bodies, and cilia (arrowhead; H), are clearly visible. (I) The magnified view of the cilium and surrounding structures. The images are shown at the following scale bars and magnifications: (G) scale bar = 5 µm; magnification: 1500×, (H) scale bar = 2 µm; magnification: 5000×, and (I) scale bar = 500 nm; magnification: 22,700×.

50% ($p < 0.05$ vs. control). This suggests that abemaciclib not only reduces cell viability but also alters EV release, potentially disrupting cellular processes related to EV production and secretion. In contrast, TMZ did not affect EV secretion, suggesting that TMZ may not influence these specific cellular mechanisms in the same way.

Both treatments led to an increase in EV size. After abemaciclib, the mean EV diameter ranged from 209 nm (day 3) to 187 nm (day 6). TMZ, on the other hand, increased EV size from 221 nm (day 3) to 191 nm (day 6). In comparison, the size of EVs from control bioprints remained relatively similar between day 3 and day 6 (153 vs. 157 nm).

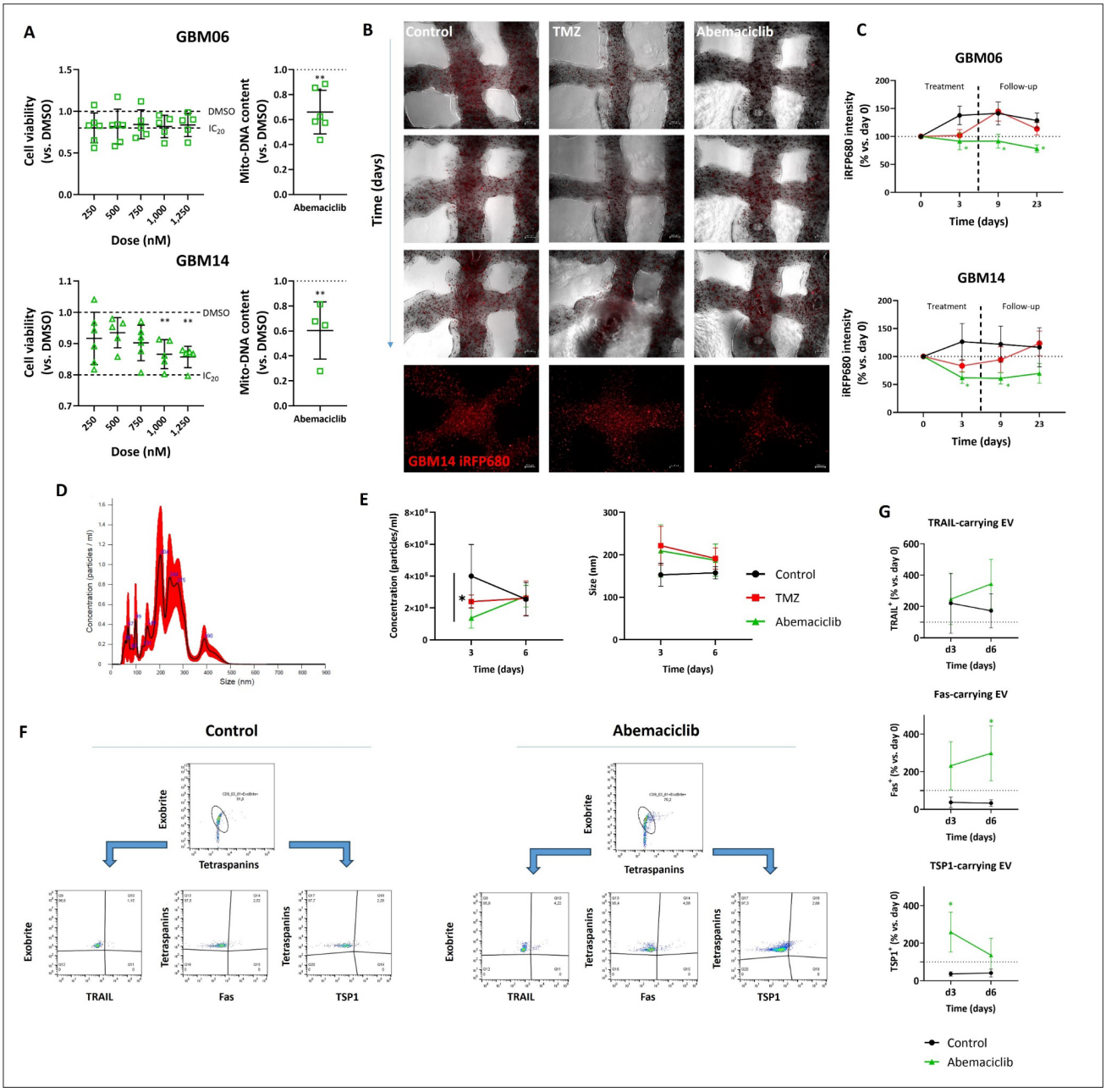


**Figure 4.** Preliminary drug testing in 2D and 3D GBM models. (A) Left: Dose–response analysis of GBM cells treated with escalating doses of abemaciclib (250–1250 nM) for two cycles of 72 h under 2D culture conditions ($n$ = 6, mean ± SD). Statistical analysis was conducted using one-way ANOVA with Dunnett's multiple comparison test (**$p < 0.01$ indicates statistical significance). Right: Mitochondrial DNA content as an indicator of cell death. Statistical analysis was conducted using an unpaired $t$-test (**$p < 0.01$ and ***$p < 0.001$ indicate statistical significance). (B, C) 3D-bioprinted cell-laden scaffolds were treated with TMZ (10 µM), abemaciclib (1 µM), or DMSO (control) for two cycles of 72 h. (B) Representative fluorescence images of treated scaffolds at different time points (scale bar = 200 µm; magnification: 3.15×). (C) Quantification of fluorescence intensity normalized to day 0 ($n$ = 7, mean ± SD). Statistical analysis was conducted using two-way ANOVA with Tukey's multiple comparison test (*$p < 0.05$ indicates statistical significance). (D, E) EV analysis in GBM14 scaffolds. Supernatants were collected at days 3 and 6 post-treatment, and EVs were isolated for quantification of particle concentration and size. (D) Representative nanoparticle tracking analysis plots. (E) Quantification of particle concentration and size ($n$ = 4, mean ± SD). Statistical analysis was conducted using two-way ANOVA with Tukey's multiple comparison test (*$p < 0.05$ indicates statistical significance). (F, G) Flow cytometric analysis of EV. (F) Gating strategy for spectral flow cytometry. (G) Quantification of specific tumor-derived EV markers. Data were normalized to day 0 (set at 100%) and expressed as relative changes at days 3 and 6. ($n$ = 3, mean ± SD). Statistical analysis was conducted using an unpaired Student's $t$-test (*$p < 0.05$ indicates statistical significance).

Abbreviations: AlgGel, alginate–gelatin; DMSO, dimethyl sulfoxide; EV, extracellular vesicle; GBM, glioblastoma; GelMa, gelatin methacryloyl; SD, standard deviation; TMZ, temozolomide; TRAIL, tumor necrosis factor-related apoptosis-inducing ligand; TSP1, thrombospondin-1.

To further confirm these findings, tumor-derived EVs from abemaciclib-treated and control scaffolds were analyzed by flow cytometry (Figure 4F and G). ExoBrite, in combination with the tetraspanins CD9, CD63, and CD81, was used as the EV-detection backbone. We then focused on markers of extrinsic, death receptor-mediated apoptosis—TRAIL and Fas. The resulting EV profile mirrored the biological effects of abemaciclib, showing increased levels of both proteins following treatment. Notably, TRAIL and Fas continued to increase over time, indicating a sustained induction of apoptotic cell death. In addition, EV-bound thrombospondin-1 (TSP1) was elevated after abemaciclib exposure. While this may reflect early ECM remodeling, we interpret the pronounced increase in TSP1-positive EVs at day 3 as an acute stress response, potentially accompanied by transient suppression of angiogenesis. Consistent with this, TSP1 levels declined by day 6.

Taken together, these findings indicate that abemaciclib substantially alters the concentration and size distribution of tumor-derived EVs, suggesting broader effects on intercellular communication and cellular stress adaptation. In contrast, TMZ did not appreciably alter EV secretion, likely reflecting its comparatively limited impact on cell viability in this model.

### 3.5. Abemaciclib selectively inhibits glioblastoma cell viability while sparing human astrocytes

GBM can evade therapeutic pressure through interactions with its surrounding microenvironment, including non-malignant cell populations. To increase the physiological relevance of our model, we incorporated hAstro cells into the previously used GBM14 monoculture (Figure 5). In this co-culture, the fluorescence signal of GBM14 cells increased steadily until day 10, reaching a 6.57-fold rise compared to day 0 (Figure 5A). Thereafter, the signal gradually declined but remained above baseline until day 28 (2.79-fold vs. day 0). The CellTrace Violet signal marking hAstro cells remained stable over the entire 28-day period (Figure 5B), indicating sustained cell viability. In contrast to the monoculture, GBM14 cells in co-culture displayed more elongated morphologies, a characteristic also observed in astrocytes (Figure 5C). Overall, both cell types remained viable and exhibited morphology consistent with adaptation to the co-culture environment.

This setting was subsequently used to assess treatment responses to abemaciclib and TMZ. Co-cultures were treated following the same schedule as monocultures (two cycles of 72 h) and monitored for 23 days. 3D confocal overviews acquired at day 21 (Figure 5D) revealed no overt morphological changes across treatment conditions. In contrast, quantitative viability measurements revealed clear treatment-dependent effects (Figure 5E and F). TMZ had no impact on GBM viability. Abemaciclib, however, significantly reduced GBM cell viability compared to controls (day 4: 300.1% vs. 393.7%; day 10: 497.9% vs. 577.2%). By day 23, the inhibitory effect was lost, with viability comparable to or exceeding controls (340.2% vs. 256.3% in controls) (Figure 5E). Importantly, astrocyte fluorescence remained unchanged following treatment with either agent (Figure 5F), indicating preserved astrocyte viability and supporting a selective inhibitory effect of abemaciclib on GBM cells.

We next evaluated the feasibility of immunofluorescence staining in the co-culture to detect treatment- or therapy-related changes (Figure 6). Two approaches were tested at day 10 after treatment initiation: (i) cryosectioning of embedded scaffolds followed by staining and (ii) direct staining of intact scaffolds. Cryosectioned samples (Figure 6A), containing unlabeled cells, were stained for astrocyte markers (e.g., S100B and ALDH1L1) and tumor markers (e.g., nestin and vimentin). Marker specificity was high, and subsets of cells exhibited co-expression. However, scaffold shrinkage during sectioning and the resulting loss of spatial context represented significant limitations. Direct staining of intact scaffolds (Figure 6B) overcame these issues. Pre-labeled cell populations enabled unambiguous cell-type discrimination, while vimentin staining highlighted tumor cells. Antibodies penetrated the hydrogels efficiently, preserving spatial organization and improving visualization within the 3D constructs.

Overall, these results demonstrate that hAstro cells can be successfully incorporated into the 3D bioprinting model without impairing GBM cell responsiveness to abemaciclib. This co-culture enhances the physiological relevance of the system while maintaining its suitability for therapeutic response assessment.

## 4. Discussion

In this study, we established a 3D bioprinting model using patient-derived GBM cells, either alone or in co-culture with hAstro cells, to perform preclinical drug response analysis. For this proof-of-concept study, the CDK4/6 inhibitor abemaciclib was used, which is currently under investigation in clinical trials for both primary and recurrent GBM.

The TME plays a critical role in GBM progression, promoting tumor cell proliferation, migration, and invasion within the brain. It is composed of multiple cellular and non-cellular components, including tumor-associated macrophages, astrocytes, the blood–brain barrier, and the hypoxic environment, all of which contribute to chemoresistance.[23–25] The intricate crosstalk

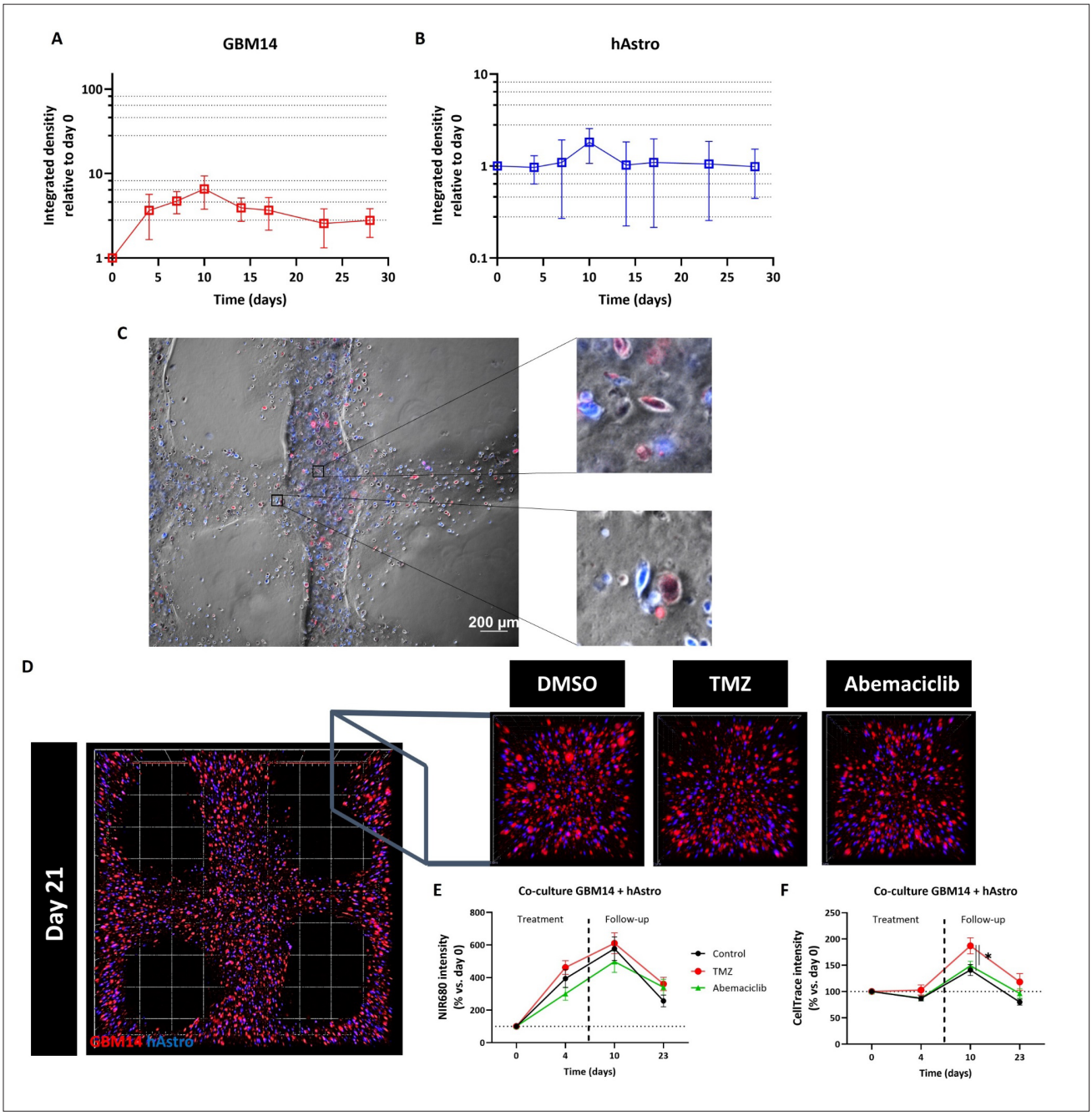


**Figure 5.** Co-culture model of GBM cells with hAstro. (A, B) The bioprinted co-culture model was treated with abemaciclib (1 µM), TMZ (10 µM), or DMSO (control) for two cycles of 72 h. (A) Fluorescence signal of iRFP680 and (B) CellTrace Violet were quantified ($n = 12$, mean ± SD). (C) Representative image of the co-cultured GBM14 cells (red) and hAstro (blue) with enlarged sections of elongated cells. (D) Scaffolds were visualized microscopically at day 21 via confocal laser scanning microscopy to generate three-dimensional images. The images were taken for the different treatment conditions. (E, F) The treatment effects were quantified based on the signal intensity of (E) iRFP680 and (F) CellTrace Violet ($n = 12$, mean ± SD). Statistical analysis was conducted using two-way ANOVA with Tukey's multiple comparison test. *$p < 0.05$ indicates statistical significance.

Abbreviations: DMSO, dimethyl sulfoxide; GBM, glioblastoma; GelMa, gelatin methacryloyl; hAstro, human astrocytes; SD, standard deviation; TMZ, temozolomide.

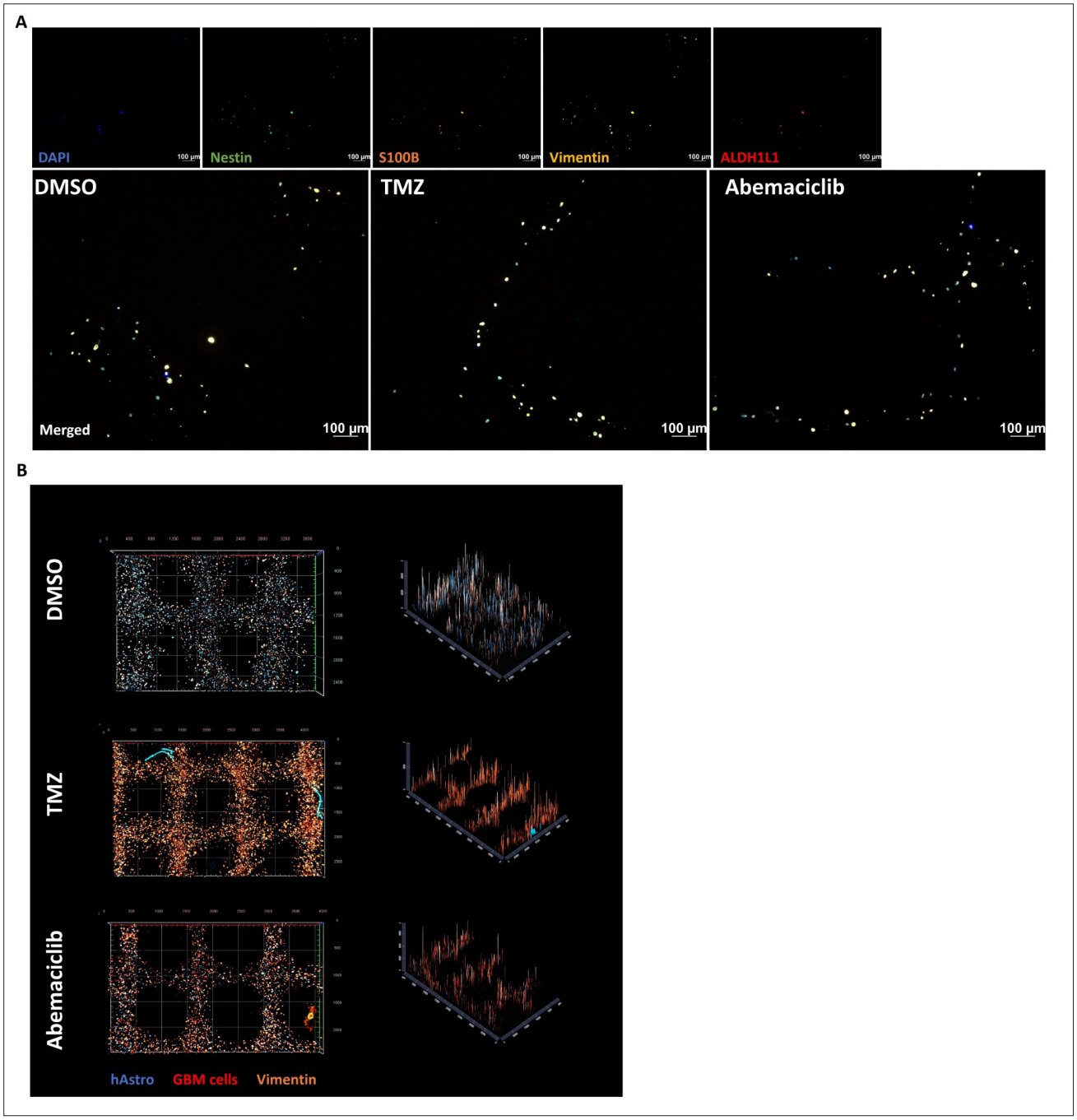


**Figure 6.** Immunofluorescence analysis of the co-culture model. (A) Bioprinted scaffolds were collected at day 10 post-treatment, embedded in TissueTek, and cryosectioned into 6-µm thick slices. Sections were stained with 4',6-diamidino-2-phenylindole (DAPI), Alexa Fluor 488 anti-nestin, DyLight 550 anti-S100B, Alexa Fluor 594 anti-vimentin, and FL650 anti-ALDH1L1 and imaged using a fluorescence microscope (scale bar = 100 µm; magnification: 6.3×). (B) Whole-mount staining of bioprinted scaffolds was performed at day 10 post-treatment. Scaffolds were stained with Alexa Fluor 594 anti-vimentin in addition to the cell-tracking stains and visualized using a confocal laser-scanning microscope.

Abbreviations: DMSO, dimethyl sulfoxide; GBM, glioblastoma; GelMa, gelatin methacryloyl; hAstro, human astrocytes; SD, standard deviation; TMZ, temozolomide.

between tumor cells and the surrounding TME presents a major barrier to effective treatment, emphasizing the need for *in vitro* models that capture this complexity.

To mimic the ECM, we used two different hydrogels—AlgGel and GelMa—both previously validated for biomimetic 3D-based approaches.[26–29] Hydrogel concentrations of 1.5% alginate/7.5% gelatin and 10% GelMa ensured a good printability of the hydrogel precursors and preservation of mechanical integrity, which are crucial for maintaining cell viability post-printing. Printability of the hydrogel is an important factor, as it directly affects cell viability and model integrity. Hydrogels that require high shear stress or elevated temperatures for printing can compromise cell viability and induce unwanted phenotypic or morphological changes.[30–32]

In our GBM model, the inclusion of gelatin as a matrix component facilitated cellular adherence and growth, largely due to the presence of the arginine–glycine–aspartic acid (RGD) motif within its amino acid sequence. The RGD motif plays a key role in mediating cell adhesion by interacting with integrin receptors on the cell surface,[33,34] thereby activating signaling pathways that are linked to cell cycle progression and, when combined with signals from growth factor receptors, promoting cell proliferation via the phosphoinositide 3-kinase/protein kinase B and extracellular signal-regulated kinase pathways.[35–37] However, since the gelatin is not covalently integrated into the network but is retained only through physical interactions (steric and electrostatic) within the ionically crosslinked hydrogel scaffold, its influence is mostly limited to the first week of culture, during which it supports GBM cell adhesion and proliferation. Over longer periods, the gelatin is expected to diffuse out of the matrix. Nonetheless, the scaffolds remained structurally stable throughout the entire cultivation period.

When comparing the two hydrogel formulations, AlgGel consistently outperformed GelMa in supporting GBM proliferation. Two of the three cell lines showed a significant increase in cell viability. EM further revealed that GBM cells in AlgGel formed microvilli-like membrane protrusions, indicative of active engagement with the surrounding matrix rather than passive encapsulation. These findings suggest that critical biophysical parameters—such as matrix density, crosslinking characteristics, and degradability—were more conducive to tumor cell growth in AlgGel.

In contrast, GelMa scaffolds did not support significant cell proliferation across the tested cell lines. This finding contrasts with previous reports demonstrating GBM growth in GelMa-based systems, including studies using GelMa/hyaluronic acid constructs co-cultured with tumor and non-tumor brain cells to mimic the TME.[38] One possible explanation for the discrepancy is the absence of additional TME components in our model, which may have limited cellular interactions and growth in GelMa. Another possibility is that, at the selected GelMa concentration, the matrix did not provide optimal biomechanical conditions for the growth of the cell line used.

Experiments involving variations in exposure time—and consequently changes in the degree of crosslinking and matrix stiffness—revealed a similar trend. Longer exposure times resulted in reduced cell viability (Figure S4). However, it remains unclear which specific biomechanical properties the ECM must exhibit to accurately mimic the TME, or to what extent these requirements depend on the individual characteristics of a given primary tumor. The literature discusses various concepts, including the notion that increased matrix stiffness reflects alterations in the TME, as both hypoxia and ECM stiffening are thought to significantly influence tumor progression. Moreover, viscoelastic parameters—such as storage modulus, loss modulus, and particularly matrix relaxation times—are likely to play a crucial role in cell fate and the development of tumor models.

Moreover, we observed an elevated background signal in GelMa-based fluorescence imaging. This may result from the UV crosslinking process, during which the photoinitiator lithium phenyl-2,4,6-trimethylbenzoylphosphinate generates free radicals to initiate GelMa polymerization. Incomplete crosslinking or residual radicals may contribute to high background noise, complicating accurate assessment of cell viability, particularly in regions with low fluorescence intensity. In contrast, AlgGel hydrogels maintain a low imaging background, offering more reliable visualization of viable cells.

The GBM15 cell line did not proliferate in either AlgGel or GelMa, likely due to insufficient adhesion within the matrix and the consequent lack of integrin-mediated survival signaling. GBM15 cells are smaller than GBM06 and GBM14 and, in 2D culture, rely on extensive cell–cell interactions and occasional spheroid formation. Thus, the initial seeding density may have been too low to support these interactions, contributing to growth arrest. These observations underscore the need to tailor cell density and matrix properties to the specific biology of each GBM line in 3D culture systems.

Recapitulating the physiological conditions of the TME is a critical aspect of effective *in vitro* modeling. Conventional 2D cultures fail to simulate the diffusion-limited nutrient and oxygen supply characteristic of tumors *in situ*, which also contributes to chemoresistance.[7,23,39] In

contrast, our 3D-bioprinted model exhibited pores within the matrix that more closely mirror *in vivo* conditions, enabling restricted but physiologically relevant diffusion of media to deeper cell layers. Importantly, bioprinted GBM cells retained their structural integrity, indicating minimal damage from the printing process. Given that 3D bioprinting can impose significant mechanical stress on cells due to extrusion pressure and shear forces,[31,32,40] this outcome suggests that our printing parameters were well-optimized to preserve cell viability and function.

After confirming cell viability and growth in AlgGel hydrogels, our patient-derived GBM model was used for preclinical drug testing. CDKs are attractive targets due to their central role in cell cycle regulation, which is frequently dysregulated in GBM.[41,42] We used the CDK4/6 inhibitor abemaciclib, whose activity against GBM was studied in our previous *in vitro* research,[14,21,22] alongside TMZ, the standard-of-care therapy. TMZ exhibited limited efficacy in our 3D model—even in the *MGMT*-methylated GBM06 line—likely reflecting microenvironment-induced drug resistance.[23,24] In contrast, abemaciclib effectively reduced growth, mitochondrial DNA content, and viability in both 2D- and 3D-cultured GBM06 and GBM14 cells.

In 2D cultures, GBM06 responded more strongly, consistent with its sensitivity due to CDK4 amplification and partial CDKN2A deletion.[22] Mechanistically, abemaciclib mimics the function of the deleted CDKN2A (encoding $p16^{INK4a}$), inhibiting CDK4/6–cyclin D binding, arresting the cell cycle at G0/G1, and inducing tumor cell death.[43]

Interestingly, in 3D cultures, both GBM lines retained sensitivity to abemaciclib, with GBM14 showing a more pronounced response than GBM06—despite lacking known CDK4/6 pathway alterations. This indicates that the 3D TME can modulate drug sensitivity in ways not captured by 2D systems, highlighting the importance of biomimetic models for preclinical research. Reduced drug efficacy in 3D likely reflects limited penetration of the drug and altered cell signaling within the hydrogel matrix.[44] To deepen our analysis, we assessed EV secretion as a functional readout of treatment response. EVs are membrane-derived vesicles secreted by cells via budding. They serve as mediators for the transfer of a variety of biomolecules to other cells and can modulate tumor growth and invasion.[45,46] Abemaciclib treatment significantly decreased EV release, while TMZ had no measurable effect—correlating with its limited therapeutic impact. Both treatments led to an increase in EV size, possibly reflecting the accumulation of bioactive cargo.

Further characterization revealed induction of apoptosis, reflected by higher levels of TRAIL and Fas on tumor-derived EVs. TRAIL and Fas act as messengers of the extrinsic apoptosis pathway, reflecting treatment-induced cell death and potentially influencing neighboring cells. Thus, the increased TRAIL and Fas on tumor-derived EVs can be interpreted as biomarkers of tumor stress. This interpretation is supported by the concurrent increase in TSP1-carrying EVs. TSP1 plays a dual role, frequently contributing to a highly invasive, immunosuppressive TME through ECM remodeling and modulation of glioma–neuron–immune crosstalk.[47] In our model, TSP1 on tumor-derived EVs was initially high, but declined rapidly, suggesting that abemaciclib exerts prolonged effects on reshaping the local TME. Collectively, these findings highlight the potential need for extended treatment regimens or combinatorial approaches to improve therapeutic efficacy. As demonstrated in our previous studies,[14,22] combination therapies may enhance the translational relevance of 3D-bioprinted GBM models, enabling more accurate prediction of clinical drug responses.

Incorporating hAstro cells into the 3D-bioprinted model increased its physiological relevance, as astrocytes are a central component of the brain microenvironment and are known to influence GBM growth, survival, and therapy resistance.[48,49] The elongated phenotypes observed in GBM cells within the co-culture likely reflect enhanced cell–cell and cell–matrix interactions mediated by astrocytes. The stable CellTrace signal indicates that astrocytes remained viable throughout the culture period, confirming the high biocompatibility of the co-culture conditions.

To our knowledge, CDK4/6 inhibition has not been evaluated in a 3D co-culture of patient-derived GBM cells and hAstro cells. In this setting, abemaciclib maintained its early inhibitory effect on GBM cell expansion without affecting astrocyte viability. Notably, after treatment cessation, GBM cells regained proliferative capacity more rapidly than in monoculture, consistent with the supportive role of astrocytes in the TME. This aligns with the known ability of GBM cells to remodel astrocytes into a reactive state that promotes tumor progression.[49] These mechanisms likely contribute to the higher overall GBM cell growth observed in the co-culture, even under treatment, and highlight the importance of incorporating astrocytes when modeling microenvironment-mediated drug resistance.

We also compared two immunofluorescence workflows to assess structural and treatment-related changes within the co-culture. Cryosectioning enabled multiplexed staining but resulted in scaffold deformation and partial loss of spatial information. In contrast, whole-mount staining preserved the 3D architecture, facilitated more reliable

visualization of cell–cell and cell–matrix interactions, and reduced variability by minimizing processing steps. Given these advantages, whole-mount staining provides a robust approach for future analyses aimed at detecting therapy-induced alterations in cellular organization or matrix composition within the bioprinted constructs.

Although this study establishes a foundational framework for patient-derived GBM models using AlgGel-based scaffolds, several limitations warrant consideration:

(i) Transient gelatin stability: Gelatin was incorporated through physical entanglement (via steric and electrostatic interactions), resulting in limited retention within the hydrogel network. Enzymatic degradation by matrix metalloproteinases further accelerates gelatin loss, thereby restricting the applicability of long-term cultures. This transient nature may influence matrix mechanics and cellular behavior over extended periods.

(ii) Matrix engineering constraints: Advanced strategies such as covalent immobilization via Schiff base chemistry or dual crosslinking approaches (e.g., microbial transglutaminase) were not implemented in the current study. These modifications could substantially alter mechanical properties, degradation kinetics, and bioactivity, and will be systematically evaluated in future work to optimize scaffold performance for long-term culture conditions.

(iii) Biological complexity and reproducibility: The use of patient-derived GBM cells enhances physiological relevance but introduces inherent heterogeneity and limits scalability compared to immortalized cell lines (e.g., U87 MG). This variability complicates the interpretation of therapeutic responses and underscores the need for standardized protocols that balance clinical fidelity with experimental reproducibility.

(iv) Analytical verification: Spectroscopic confirmation of gelatin retention (e.g., FTIR detection of amide bands at around 1650 and 1540 $cm^{-1}$) was not feasible for individualized cell line experiments. Future studies should incorporate robust analytical workflows to monitor matrix integrity and biochemical composition over time.

Despite these constraints, the current platform provided sufficient structural stability for initial bioprinting, cell viability, and drug screening assays. Moving forward, integrating advanced crosslinking chemistries, quantitative matrix characterization, and comparative analyses across cell sources will be critical for establishing predictive, clinically relevant GBM models.

## 5. Conclusion

This study presents a robust 3D bioprinting platform incorporating patient-derived GBM cells within biomimetic hydrogels, successfully replicating key features of the native TME. The model supports longitudinal analysis of cell viability, therapeutic response, and EV secretion, demonstrating its relevance for preclinical drug screening. The performance of the AlgGel hydrogel and the efficacy of abemaciclib indicate that the platform can capture tumor-specific responses not observable in conventional 2D models. The co-culture with astrocytes further enhances the physiological relevance of the model without compromising treatment responsiveness. These findings highlight the model's capacity to reveal clinically relevant, tumor-specific behaviors. While further integration of TME components is needed, this model represents a valuable step toward more predictive *in vitro* drug testing and the development of personalized therapeutic strategies for GBM.

## Acknowledgments

We thank Ute Schulz and Dr. Armin Springer for excellent technical support during EM sample preparation at the Electron Microscopy Centre.

## Funding

The project was funded by the German Federal Institute for Risk Assessment Grant Agreement Number 60-0102-01.P640 to C.M. and C.P. and by Deutsche Forschungsgemeinschaft (DFG, German Research Foundation) – SFB 1270/1,2–299150580 to H.S.

## Conflict of interest

The authors declare that the research was conducted in the absence of any commercial or financial relationships that could be construed as a potential conflict of interest.

## Author contributions

*Conceptualization:* Christian Polley, Claudia Maletzki
*Data curation:* Philipp Kaps, Emily Zunke, Justus Ramtke
*Formal analysis:* Philipp Kaps, Emily Zunke, Justus Ramtke
*Funding acquisition:* Christian Polley, Hermann Seitz, Claudia Maletzki
*Investigation:* Philipp Kaps, Emily Zunke, Justus Ramtke, Charlotte Wagner, Annabell Wolff, Christian Polley, Leonora Calopresti, Marcus Frank, Karoline Schulz
*Methodology:* Philipp Kaps, Emily Zunke, Justus Ramtke, Leonora Calopresti, Charlotte Wagner, Annabell Wolff, Marcus Frank, Karoline Schulz

*Project administration:* Claudia Maletzki, Christian Polley, Hermann Seitz
*Resources:* Claudia Maletzki, Hermann Seitz, Christian Junghanss, Daniel Dubinski, Florian Gessler, Thomas Freiman, Piotr Grabarczyk, Sascha Troschke-Meurer
*Validation:* Claudia Maletzki
*Visualization:* Philipp Kaps, Emily Zunke, Justus Ramtke
*Supervision:* Claudia Maletzki, Hermann Seitz, Christian Junghanss
*Writing–original draft:* Philipp Kaps, Claudia Maletzki
*Writing–review & editing:* All authors

## Ethics approval and consent to participate

All cell lines used in this study were originally established from tumor tissue obtained with written informed consent from the patients. All procedures were approved by the Ethics Committee of the Rostock University Medical Center, University of Rostock (Ethikkommission an der Medizinischen Fakultät der Universität Rostock, St.-Georg-Str. 108, 18055 Rostock, Germany; Ethics Registration ID: A2018-0167) and were conducted in accordance with generally accepted guidelines for the use of human material.

## Consent for publication

Not applicable.

## Availability of data

Data are available from the corresponding author upon reasonable request.

## Further disclosure

Part of the findings were presented at the Annual European Society for Medical Oncology Congress (17-21 October 2025 at the Messe Berlin) under the title: Modeling the glioblastoma microenvironment with 3D bioprinting for preclinical evaluation of CDK4/6 inhibition.

## References


1. Ostrom QT, Cioffi G, Waite K, Kruchko C, Barnholtz-Sloan JS. CBTRUS statistical report: primary brain and other central nervous system tumors diagnosed in the United States in 2014–2018. *Neuro Oncol*. 2021;23(Suppl 3):iii1. doi: 10.1093/NEUONC/NOAB200
2. Weller M, Wen PY, Chang SM, *et al*. Glioma. *Nat Rev Dis Primers*. 2024;10(1):33. doi: 10.1038/S41572-024-00516-Y
3. Hughes JP, Rees SS, Kalindjian SB, Philpott KL. Principles of early drug discovery. *Br J Pharmacol*. 2011;162(6):1239-1249. doi: 10.1111/J.1476-5381.2010.01127.X
4. Knight E, Przyborski S. Advances in 3D cell culture technologies enabling tissue-like structures to be created in vitro. *J Anat*. 2015;227(6):746-756. doi: 10.1111/JOA.12257
5. Costa EC, Moreira AF, de Melo-Diogo D, Gaspar VM, Carvalho MP, Correia IJ. 3D tumor spheroids: an overview on the tools and techniques used for their analysis. *Biotechnol Adv*. 2016;34(8):1427-1441. doi: 10.1016/J.BIOTECHADV.2016.11.002
6. Ravi M, Paramesh V, Kaviya SR, Anuradha E, Paul Solomon FD. 3D cell culture systems: advantages and applications. *J Cell Physiol*. 2015;230(1):16-26. doi: 10.1002/JCP.24683
7. Jensen C, Teng Y. Is it time to start transitioning from 2D to 3D cell culture? *Front Mol Biosci*. 2020;7:3. doi: 10.3389/FMOLB.2020.00033
8. Ozbolat IT, Peng W, Ozbolat V. Application areas of 3D bioprinting. *Drug Discov Today*. 2016;21(8):1257-1271. doi: 10.1016/J.DRUDIS.2016.04.006
9. Gungor-Ozkerim PS, Inci I, Zhang YS, Khademhosseini A, Dokmeci MR. Bioinks for 3D bioprinting: an overview. *Biomater Sci*. 2018;6(5):915-946. doi: 10.1039/C7BM00765E
10. Han S, Kim S, Chen Z, *et al*. 3D bioprinted vascularized tumour for drug testing. *Int J Mol Sci*. 2020;21(8):2993. doi: 10.3390/IJMS21082993
11. Bo T, Pascucci E, Capuani S, *et al*. 3D bioprinted mesenchymal stem cell laden scaffold enhances subcutaneous vascularization for delivery of cell therapy. *Biomed Microdevices*. 2024;26(3):29. doi: 10.1007/S10544-024-00713-2
12. Forkel H, Grabarczyk P, Depke M, *et al*. BCL11B depletion induces the development of highly cytotoxic innate T cells out of IL-15 stimulated peripheral blood αβ CD8+ T cells. *Oncoimmunology*. 2022;11(1):2148850. doi: 10.1080/2162402X.2022.2148850
13. Troschke-Meurer S, Zumpe M, Meißner L, *et al*. Chemotherapeutics used for high-risk neuroblastoma therapy improve the efficacy of anti-GD2 antibody dinutuximab beta in preclinical spheroid models. *Cancers (Basel)*. 2023;15(3):904. doi: 10.3390/CANCERS15030904
14. Riess C, del Moral K, Fiebig A, *et al*. Implementation of a combined CDK inhibition and arginine-deprivation approach to target arginine-auxotrophic glioblastoma multiforme cells. *Cell Death Dis*. 2022;13(6):555. doi: 10.1038/s41419-022-05006-1
15. Kayser A, Wolff A, Berlin P, *et al*. Selective but not pan-CDK inhibition abrogates 5-FU-driven tissue factor upregulation in colon cancer. *Sci Rep*. 2024;14(1):1-12. doi: 10.1038/s41598-024-61076-5

16. Amorim PA, d'Ávila MA, Anand R, Moldenaers P, Van Puyvelde P, Bloemen V. Insights on shear rheology of inks for extrusion-based 3D bioprinting. *Bioprinting*. 2021;22:e00129.
doi: 10.1016/J.BPRINT.2021.E00129

17. Naghieh S, Chen X. Printability–a key issue in extrusion-based bioprinting. *J Pharm Anal*. 2021;11(5):564-579.
doi: 10.1016/J.JPHA.2021.02.001

18. Habib MA, Khoda B. Rheological analysis of bio-ink for 3D bio-printing processes. *J Manuf Process*. 2022;76:708-718.
doi: 10.1016/J.JMAPRO.2022.02.048

19. Hull SM, Brunel LG, Heilshorn SC. 3D bioprinting of cell-laden hydrogels for improved biological functionality. *Adv Mater*. 2022;34(2):2103691.
doi: 10.1002/ADMA.202103691

20. Gao T, Gillispie GJ, Copus JS, *et al*. Optimization of gelatin-alginate composite bioink printability using rheological parameters: a systematic approach. *Biofabrication*. 2018;10(3):034106.
doi: 10.1088/1758-5090/AACDC7

21. Riess C, Koczan D, Schneider B, *et al*. Cyclin-dependent kinase inhibitors exert distinct effects on patient-derived 2D and 3D glioblastoma cell culture models. *Cell Death Discov*. 2021;7(1):54.
doi: 10.1038/s41420-021-00423-1

22. Freitag T, Kaps P, Ramtke J, *et al*. Combined inhibition of EZH2 and CDK4/6 perturbs endoplasmic reticulum-mitochondrial homeostasis and increases antitumor activity against glioblastoma. *NPJ Precis Oncol*. 2024;8(1):156.
doi: 10.1038/S41698-024-00653-3

23. Da Ros M, De Gregorio V, Iorio AL, *et al*. Glioblastoma chemoresistance: the double play by microenvironment and blood-brain barrier. *Int J Mol Sci*. 2018;19(10):2879.
doi: 10.3390/IJMS19102879

24. Zhang X, Ding K, Wang J, Li X, Zhao P. Chemoresistance caused by the microenvironment of glioblastoma and the corresponding solutions. *Biomed Pharmacother*. 2019;109:39-46.
doi: 10.1016/J.BIOPHA.2018.10.063

25. Perrin SL, Samuel MS, Koszyca B, *et al*. Glioblastoma heterogeneity and the tumour microenvironment: implications for preclinical research and development of new treatments. *Biochem Soc Trans*. 2019;47(2):625-638.
doi: 10.1042/BST20180444

26. Giuseppe M Di, Law N, Webb B, *et al*. Mechanical behaviour of alginate-gelatin hydrogels for 3D bioprinting. *J Mech Behav Biomed Mater*. 2018;79:150-157.
doi: 10.1016/J.JMBBM.2017.12.018

27. Liu P, Shen H, Zhi Y, *et al*. 3D bioprinting and in vitro study of bilayered membranous construct with human cells-laden alginate/gelatin composite hydrogels. *Colloids Surf B Biointerfaces*. 2019;181:1026-1034.
doi: 10.1016/J.COLSURFB.2019.06.069

28. Yin J, Yan M, Wang Y, Fu J, Suo H. 3D bioprinting of low-concentration cell-laden gelatin methacrylate (GelMA) bioinks with a two-step cross-linking strategy. *ACS Appl Mater Interfaces*. 2018;10(8):6849-6857.
doi: 10.1021/ACSAMI.7B16059

29. Cuvellier M, Ezan F, Oliveira H, *et al*. 3D culture of HepaRG cells in GelMa and its application to bioprinting of a multicellular hepatic model. *Biomaterials*. 2021;269:120611.
doi: 10.1016/J.BIOMATERIALS.2020.120611

30. Nair K, Gandhi M, Khalil S, *et al*. Characterization of cell viability during bioprinting processes. *Biotechnol J*. 2009;4(8):1168-1177.
doi: 10.1002/BIOT.200900004

31. Boularaoui S, Al Hussein G, Khan KA, Christoforou N, Stefanini C. An overview of extrusion-based bioprinting with a focus on induced shear stress and its effect on cell viability. *Bioprinting*. 2020;20:e00093.
doi: 10.1016/J.BPRINT.2020.E00093

32. Adhikari J, Roy A, Das A, *et al*. Effects of processing parameters of 3D bioprinting on the cellular activity of bioinks. *Macromol Biosci*. 2021;21(1):2000179.
doi: 10.1002/MABI.202000179

33. Davidenko N, Schuster CF, Bax DV, *et al*. Evaluation of cell binding to collagen and gelatin: a study of theeffect of 2D and 3D architecture and surface chemistry. *J Mater Sci Mater Med*. 2016;27(10):148.
doi: 10.1007/S10856-016-5763-9

34. Su K, Wang C. Recent advances in the use of gelatin in biomedical research. *Biotechnol Lett*. 2015;37(11):2139-2145.
doi: 10.1007/S10529-015-1907-0

35. Streulli CH, Akhtar N. Signal co-operation between integrins and other receptor systems. *Biochem J*. 2009;418(3):491-506.
doi: 10.1042/BJ20081948

36. Jeanes AI, Wang P, Moreno-Layseca P, *et al*. Specific β-containing integrins exert differential control on proliferation and two-dimensional collective cell migration in mammary epithelial cells. *J Biol Chem*. 2012;287(29):24103-24112.
doi: 10.1074/JBC.M112.360834

37. Moreno-Layseca P, Streuli CH. Signalling pathways linking integrins with cell cycle progression. *Matrix Biol*. 2014;34:144-153.
doi: 10.1016/J.MATBIO.2013.10.011

38. Tang M, Xie Q, Gimple RC, *et al*. Three-dimensional bioprinted glioblastoma microenvironments model cellular dependencies and immune interactions. *Cell Res*. 2020;30(10):833-853.
doi: 10.1038/s41422-020-0338-1

39. Li DM, Chen QD, Wei GN, *et al*. Hypoxia-induced miR-137 inhibition increased glioblastoma multiforme growth and chemoresistance through LRP6. *Front Oncol*. 2021;10:611699.
doi: 10.3389/FONC.2020.611699

40. Blaeser A, Filipa Duarte Campos D, Puster U, *et al*. Controlling shear stress in 3D bioprinting is a key factor to balance printing resolution and stem cell integrity. *Adv Healthc Mater*. 2016;5(3):326-333. doi: 10.1002/ADHM.201500677

41. Hanahan D, Weinberg RAA. Hallmarks of cancer: the next generation. *Cell*. 2011;144(5):646-674. doi: 10.1016/j.cell.2011.02.013

42. Koo H, Choi SW, Cho HJ, *et al*. Ethnic delineation of primary glioblastoma genome. *Cancer Med*. 2020;9(19):7352. doi: 10.1002/CAM4.3370

43. Zhao R, Choi BY, Lee MH, Bode AM, Dong Z. Implications of genetic and epigenetic alterations of CDKN2A (p16INK4a) in cancer. *EBioMedicine*. 2016;8:30-39. doi: 10.1016/J.EBIOM.2016.04.017

44. Fontoura JC, Viezzer C, dos Santos FG, *et al*. Comparison of 2D and 3D cell culture models for cell growth, gene expression and drug resistance. *Mater Sci Eng C*. 2020;107:110264. doi: 10.1016/J.MSEC.2019.110264

45. Mulcahy LA, Pink RC, Carter DRF. Routes and mechanisms of extracellular vesicle uptake. *J Extracell Vesicles*. 2014;3(1):24641. doi: 10.3402/JEV.V3.24641

46. Raposo G, Stoorvogel W. Extracellular vesicles: exosomes, microvesicles, and friends. *J Cell Biol*. 2013;200(4):373-383. doi: 10.1083/JCB.201211138

47. Nejo T, Krishna S, Yamamichi A, *et al*. Glioma-neuronal circuit remodeling induces regional immunosuppression. *Nat Commun*. 2025;16(1):4770. doi: 10.1038/s41467-025-60074-z

48. Brandao M, Simon T, Critchley G, Giamas G. Astrocytes, the rising stars of the glioblastoma microenvironment. *Glia*. 2019;67(5):779-790. doi: 10.1002/glia.23520

49. Mega A, Hartmark Nilsen M, Leiss LW, *et al*. Astrocytes enhance glioblastoma growth. *Glia*. 2020;68(2):316-327. doi: 10.1002/glia.23718